Running title: An endocytic myosin-1 generates power

Power generation by a myosin-1 essential for endocytosis: implications for biological mechanism

Ross TA Pedersen[1, 3, 4], Aaron Snoberger[2, 4], Serapion Pyrpassopoulos[2], Daniel Safer[2], David G Drubin[1*], E Michael Ostap[2*]

[1]Department of Molecular and Cell Biology, University of California, Berkeley, Berkeley, CA 94720

[2]Pennsylvania Muscle Institute, Perelman School of Medicine, University of Pennsylvania, Philadelphia, PA 19104

[3]Present address: Department of Embryology, Carnegie Institution for Science, Baltimore, MD 21218

[4]Equal Contribution

*Correspondence: drubin@berkeley.edu, ostap@mail.med.upenn.edu

16 **Summary**

17

18 Pedersen, Snoberger et al. measure the force-sensitivity of the yeast endocytic the myosin-
19 1 called Myo5 and find that it is more likely to generate power than to serve as a force-
20 sensitive anchor in cells. Implications for Myo5's role in clathrin-mediated endocytosis are
21 discussed.

22 **Abstract**

23 Myosins are required for clathrin-mediated endocytosis, but their precise molecular roles
24 in this process are not known. This is, in part, because the biophysical properties of the
25 relevant motors have not been investigated. Myosins have diverse mechanochemical
26 activities, ranging from powerful contractility against mechanical loads to force-sensitive
27 anchoring. To better understand the essential molecular contribution of myosin to
28 endocytosis, we studied the in vitro force-dependent kinetics of the *Saccharomyces*
29 *cerevisiae* endocytic type I myosin called Myo5, a motor whose role in clathrin-mediated
30 endocytosis has been meticulously studied in vivo. We report that Myo5 is a low-duty-ratio
31 motor that is activated ~10-fold by phosphorylation, and that its working stroke and actin-
32 detachment kinetics are relatively force-insensitive. Strikingly, the in vitro
33 mechanochemistry of Myo5 is more like that of cardiac myosin than like that of slow
34 anchoring myosin-1s found on endosomal membranes. We therefore propose that Myo5
35 generates power to augment actin assembly-based forces during endocytosis in cells.

36 **Introduction**

37

38 During clathrin-mediated endocytosis (CME), the plasma membrane invaginates and
39 undergoes scission to become a cytoplasmic vesicle. Coat proteins like clathrin can deform
40 membranes under low tension (Dannhauser and Ungewickell, 2012; Busch et al., 2015; Cail
41 et al., 2022), but when membrane bending is resisted by membrane tension (Hassinger et
42 al., 2017), the actin cytoskeleton drives plasma membrane invagination (Boulant et al.,
43 2011; Kaplan et al., 2022). In yeasts, including *Saccharomyces cerevisiae* and
44 *Schizosaccharomyces pombe*, turgor pressure opposes plasma membrane invagination, so
45 actin is required at every CME site (Aghamohammadzadeh and Ayscough, 2009; Basu et al.,
46 2013).

47 The actin cytoskeleton can produce pushing and pulling force, both of which are
48 required for CME in *S. cerevisiae* (Sun et al., 2006). When actin filament ends grow against a
49 surface, they push the surface forward (Mogilner and Oster, 1996, 2003). During CME, actin
50 filaments, bound by coat proteins, grow against the plasma membrane at the base the CME
51 site, driving invagination (Picco et al., 2015; Kaksonen et al., 2005, 2003; Skruzny et al., 2012,
52 Fig. 1). Modeling of the homologous CME machinery in mammalian cells has demonstrated
53 that such actin networks generate sufficient power for CME (Akamatsu et al., 2020), but
54 whether actin assembly alone can overcome turgor pressure in yeast cells is under debate
55 (Nickaeen et al., 2019; Carlsson, 2018).

56 Additional power may be provided by myosins, which generate tension on actin
57 filaments. The myosins critical for CME, Myo3 and Myo5 in budding yeast, and Myo1e in
58 vertebrates, are type I myosins (Geli and Riezman, 1996; Cheng et al., 2012; Krendel et al.,

59 2007). Some type I myosins are well-suited to generate power – i.e., they carry out
60 mechanical work per unit time by consuming ATP to execute a power stroke. Other type I
61 myosins are ideally suited to serve as force-sensitive anchors – their ATPase cycle is easily
62 arrested by resistance, locking them in a state that maintains tension without completing the
63 ATPase cycle or powering movement (Greenberg and Ostap, 2013). The possible roles of
64 type I myosins in CME depend on whether endocytic myosins are power generators or force-
65 sensitive anchors.

66 If endocytic type I myosins are acutely force-sensitive, they might organize the actin
67 filaments of the endocytic actin network, while if they are less force sensitive, they could
68 power plasma membrane invagination (Evangelista et al., 2000, Fig. 1). Myosin-1 motors
69 form a ring at the base of CME sites, where the invaginated membrane meets the plasma
70 membrane (Mund et al., 2018, Fig. 1). Yeast type I myosins serve at least one organizational
71 function as a membrane anchor for the actin assembly machinery, a function associated
72 with the non-motor tail of the molecules (Lewellyn et al., 2015), but motor activity is
73 required in addition to membrane anchorage (Pedersen and Drubin, 2019). If endocytic
74 myosin-1s are force sensitive anchors, they may serve a further organizational role by
75 holding growing filaments in an optimal orientation for force generation (Fig. 1, left). If the
76 myosins are power-generating motors, they may pull actin filament ends away from the
77 plasma membrane, deepening the plasma membrane invagination and creating space for
78 monomer addition and filament elongation (Fig. 1, right), a model supported by the
79 observation that the actin assembly rate at CME sites depends on type I myosin motors in a
80 dose-dependent manner (Manenschijn et al., 2019).

81 To distinguish between these possibilities, we measured the force sensitivity of the
82 endocytic myosin Myo5 (not to be confused with the vertebrate type V myosin). Myo5 is
83 insensitive to resistive force compared to related myosins. We therefore propose that Myo5
84 actively powers CME. Because actin and myosin collaborate in a variety of membrane
85 remodeling processes, we expect that these results will be instructive beyond CME.

86 **Results and Discussion**

87

88 **Heavy Chain Phosphorylation Activates Myo5 ATPase Activity**

89 To determine how force sensitive Myo5 is, we first needed to measure its unloaded
90 kinetics. We purified a Myo5 construct containing the motor and lever domains from *S.*
91 *cerevisiae* (Fig. 2A). Because phosphorylation of Myo5 at the TEDS site is required for most
92 CME events and is thought to regulate Myo5's motor activity (Grosshans et al., 2006; Sun et
93 al., 2006; Bement and Mooseker, 1995), we purified a phosphorylated version and an
94 unphosphorylated version of the protein separately (See Materials and methods). p21
95 activated kinase was used to phosphorylate the myosin at the TEDS site (S357), as
96 determined by control experiments with an S357A mutant (Fig. S1). The phosphorylation
97 state of preparations was judged to be uniform when ATP-induced actoMyo5 dissociation
98 transients were well fit by single exponential functions (see below). The yeast light chain
99 for Myo5, calmodulin (Cmd1, Geli et al., 1998) was purified from *E. coli* and included in
100 excess in all experiments (Fig. 2A).

101 We measured the steady-state actin-activated ATPase activities of phosphorylated
102 and unphosphorylated Myo5 using the NADH-coupled assay (De La Cruz and Ostap, 2009)
103 in the presence of 0 - 80 μM phalloidin-stabilized actin. Unphosphorylated Myo5 ATPase
104 activity was largely insensitive to actin: the ATPase rate for at 0 μM actin was 0.14 s^{-1}, while
105 the maximum ATPase rate measured was 0.39 s^{-1} at 40 μM actin. (Fig. 2B). Phosphorylation
106 activated Myo5 ATPase activity by about 10-fold (Fig. 2B). The actin concentration
107 dependence of the phosphorylated Myo5 ATPase rate (k_{obs}) was well fit by:

108 $$k_{obs} = v_o \frac{V_{\max}[Actin]}{K_{\mathrm{ATPase}}+[Actin]} \qquad \textbf{(Equation 1)}$$

109 From the fit, the actin concentration at half-maximum of the ATPase rate (K_{ATPase}) was
110 determined to be 5.1 ± 0.88 μM, and the maximum ATPase rate (V_{max}) was found to be 3.3 ±
111 0.15 s^{-1} (Fig, 2B; Table 1).
112

113 **ATP Binding and ADP Release are Non-Rate Limiting for Myo5 ATPase Activity**

114 Resistive force impacts the rate of myosin detachment from actin, and two biochemical
115 transitions, ADP release and subsequent ATP binding, determine the detachment rate.
116 Therefore, we used stopped-flow kinetics to measure ADP release from (Fig. 2C, k_{+5}') and
117 ATP binding to (Fig. 2C, K_1' and k_{+2}') actoMyo5.
118 We found that yeast Myo5 does not quench the fluorescence of actin labeled at cys-374
119 with pyrene iodoacetamide, which is the probe most used to measure actomyosin
120 attachment and detachment (De La Cruz and Ostap, 2009). Thus, we measured actoMyo5
121 detachment by monitoring light scattering, which decreases as myosin unbinds actin.
122 To determine the rate constant for ATP binding, we mixed nucleotide-free actoMyo5
123 (100 nM) with varying concentrations of ATP and monitored 90° light scattering in the
124 stopped flow instrument. Light scattering time courses followed single exponential
125 functions (Fig 2D). For phosphorylated Myo5, the observed rates determined from the fits
126 increased linearly with ATP concentration (Fig. 2E). At concentrations of > 1 mM ATP, the
127 actomyosin complex dissociated within the response time of the instrument, precluding
128 measurement. For unphosphorylated Myo5, the observed rates fit a rectangular hyperbola
129 with increasing ATP concentration (Fig. 2E).

130 The mechanism was modeled as (De La Cruz and Ostap, 2009):

131 $$K_1' \qquad k_2' \qquad k_{diss}$$

132 $$AM + ATP \rightleftharpoons AM(ATP) \longrightarrow AM.ATP \longrightarrow A + M.ATP\,, \quad \textbf{(Scheme 1)}$$

133 where K_1' is a rapid equilibrium binding step, k_2' is a rate-limiting isomerization to the
134 AM.ATP state, and k_{diss} is the rapid actin dissociation step. The apparent second order rate
135 constant for ATP binding to phosphorylated actoMyo5 was determined by a linear fit to the
136 data ($K_1'k_2'$ = 0.39 ± 0.017 μm^{-1} s^{-1}). The unphosphorylated actoMyo5 data were fit by:

137 $$k_{obs} = \left[\frac{K_1'\,[ATP]}{1+K_1'\,[ATP]}\right] k_2'\,, \qquad \textbf{(Equation 2)}$$

138 and the maximum rate of isomerization (k_2' = 290 ± 24 s^{-1}) and ATP affinity (K_1' = 0.006 ±
139 0.0016 μM^{-1}) were determined. The apparent second-order rate constant for ATP binding
140 ($K_1'k_2'$) was determined from a linear fit of the observed rates below 100 μM ATP to be 1.1
141 ± 0.28 μM^{-1} s^{-1} (Table 1).

142 The rate constant for ADP dissociation (k_{+5}') was measured by preincubating
143 100 μM ADP with 200 nM actoMyo5 and then rapidly mixing with 2.5 mM ATP as shown in
144 **scheme 2**:

145 $$k_5'$$

146 $$A.M.ADP \rightleftharpoons A.M + ATP \rightleftharpoons A.M(ATP) \longrightarrow A + M.ATP\,, \quad \textbf{(Scheme 2)}$$

147 When myosin active sites are saturated with ADP, the rate of ATP-induced dissociation of
148 actomyosin is limited by ADP's slow dissociation. Light scattering transients were fitted by
149 single exponential functions, yielding rates for ADP release for phosphorylated actoMyo5
150 (k_{+5}' = 74 ± 2.0s^{-1}) and for unphosphorylated actoMyo5 (k_{+5}' = 107 ± 5.9 s^{-1}) (Fig. 2F and
151 Table 1). The signal-to-noise ratio of the fast light scattering transients is low, resulting in
152 large uncertainties on these fits. However, these rates are substantially faster than the

153 steady-state ATPase values, but slower than the maximum rate of ATP-induced actomyosin
154 dissociation. ADP release for actoMyo5 ADP is much faster than ADP release for vertebrate
155 Myo1b and Myo1c (Greenberg et al., 2012; Lewis et al., 2006). It is more similar to the
156 vertebrate endocytic myosin-1, Myo1e (El Mezgueldi et al., 2002). Because ADP release is
157 rate limiting for detachment of Myo5 and Myo1e from actin, fast ADP release by these
158 molecules mean that the unloaded actin-attachment lifetimes for endocytic type I myosins
159 are < 15 ms. This property may make these motors particularly well-suited to function in
160 dynamic actin networks like those at CME sites, where actin filaments elongate and
161 "treadmill" into the cytoplasm (Kaksonen et al., 2003, 2005).
162

163 **Actin gliding is dependent on Myo5 phosphorylation state**

164 Our kinetic results suggest that both phosphorylated and unphosphorylated Myo5 have
165 low duty ratios (i.e., the motor spends a small fraction of its ATPase cycle bound to actin).
166 Since ADP release limits the rate of phosphorylated Myo5 detachment from actin at
167 saturating ATP (k_{+5}' = 74 ± 2.0 s^{-1}) and since we have measured the overall ATPase rate
168 (V_{max} = 3.3 ± 0.15 s^{-1}), we can estimate the duty ratio:

169 $$Duty\ Ratio = \frac{(\frac{1}{k'_5})}{(\frac{1}{Vmax})}, \qquad \textbf{(Equation 3)}$$

170 The calculated duty ratio of phosphorylated Myo5 is 0.045. Unphosphorylated Myo5 has a
171 lower duty ratio (< 0.004).

172 To assess the effect of phosphorylation on Myo5 motility, we performed in vitro
173 motility assays at 1 mM ATP. Motors were attached site-specifically to coverslips coated
174 with anti-His_6 antibody. Coverslips were incubated with a range of concentrations of

175 phosphorylated and unphosphorylated Myo5, creating a titration series of surface
176 densities. At low Myo5 surface densities (incubation with ≤ 30 nM phosphorylated Myo5,
177 ≤ 150 nM unphosphorylated Myo5), actin filaments failed to bind the coverslip (Fig. 2G and
178 movies S1 and S2). At higher concentrations, phosphorylated Myo5 moved actin filaments
179 at velocities ranging from 720 ± 40 nm/s (100 nM phosphorylated Myo5) to 880 ± 90 nm/s
180 (40 nM) (Fig. 2G and movie S1). These gliding velocities are considerably higher than those
181 reported by Sun et al., 2006, possibly reflecting differences in the phosphorylation state of
182 the purified Myo5 protein (see below) or differences in other motility assay conditions,
183 such as light chain availability. Higher (> 5-fold) surface densities of unphosphorylated
184 Myo5 were required to achieve smooth motility, but this motility occurred at a
185 substantially slower speed, ~120 nm/s (Fig. 2G and movie S2). While it is possible that
186 residual phosphorylated Myo5 in the unphosphorylated prep contributed to this motility,
187 Sun et al., 2006 similarly reported that Myo5 harboring TEDS site mutations moved actin
188 filaments much more slowly. The slower actin gliding speed for unphosphorylated myosin
189 was unexpected given the similar rates of ADP release between phosphorylated and
190 unphosphorylated Myo5 (Table 1). It is possible that the our kinetics experiments have not
191 determined the rate limiting step for detachment, but it is more likely that motility of the
192 unphosphorylated myosin is limited by the slow attachment rate of the motor (Stewart et
193 al., 2021), as suggested by the slow actin-activated ATPase rate. The activation of Myo5
194 motility by phosphorylation could explain why fast, cargo-induced endocytosis, which
195 involves rapid and dynamic actin turnover, requires phosphorylated Myo5, while slower
196 constitutive endocytosis does not (Grosshans et al., 2006).
197

198 **Myo5's working stroke comprises two substeps that are consistent with unloaded**
199 **kinetic measurements**

200 The kinetics of actin attachment durations and mechanics of single myosin molecules were
201 measured using an optical trapping instrument that can detect sub-nanometer
202 displacements with millisecond temporal resolution (Woody et al., 2018; Snoberger et al.,
203 2021). We used the three-bead optical trapping geometry in which a biotinylated actin
204 filament is held between two laser-trapped polystyrene beads coated with neutravidin,
205 creating a bead-actin-bead dumbbell (Fig. 3A). Dumbbells were lowered onto pedestal
206 beads that were sparsely coated with phosphorylated Myo5-His_9 bound to a surface-
207 adsorbed anti-His_6 tag antibody. The positions of trapped beads were detected via
208 quadrant photodiode detectors, and single actomyosin binding events were detected by the
209 decrease in covariance of the positions of the two dumbbell beads (Fig. 3B-D).

210 Traces acquired at 1, 10, and 1000 μM ATP reveal displacements and drops in
211 covariance during actomyosin binding events. Individual points from covariance traces
212 were fit by double gaussian distributions, with the thresholds for event detection indicated
213 as dotted gray lines in Fig. 3 B-D. Event durations decreased with increasing ATP
214 concentrations (Fig. 3 B-D, blue lines).

215 The myosin-1 working stroke has been shown to occur in two discrete substeps,
216 with the first substep occurring with actin-activated phosphate release, and the second
217 occurring with ADP release (Jontes et al., 1995; Veigel et al., 1999, Fig. 3E). The substeps
218 can be characterized in optical trapping assays by ensemble averaging single interactions
219 (Veigel et al., 1999; Chen et al., 2012; Laakso et al., 2008), where the detected events are

220 aligned at their beginnings and forward-averaged in time (Fig 3F-H, left), or aligned at their
221 ends and reverse-averaged in time (Fig 3F-H, right).

222 Ensemble averages of Myo5 interactions showed a two-step working stroke at the
223 three ATP concentrations, but the step-size was most accurately resolved at 10 μM ATP
224 (see Materials and methods). In this condition, an initial substep of 4.8 nm was followed by
225 a second substep of 0.2 nm (Fig. 3G). We determined the lifetimes of the substeps by fitting
226 the ensemble averages with single exponential functions. At 1 μM ATP (Fig. 3F, left trace),
227 the measured rate (> 30 s^{-1}) of the time-forward average was limited by the covariance
228 smoothing window, but at 10 and 1000 μM ATP (Fig. 3 G-H, left traces), the rates were 49 ±
229 1.6 and 50 ± 0.2 s^{-1}, respectively (Fig. 3K) which are similar to the measured ADP release
230 rate (k_{+5}', 74 ± 2.0 s^{-1}, Table 1) supporting the model that the transition from state-1 to
231 state-2 accompanies ADP release.

232 The kinetics of time-reversed averages reveal the lifetime of State 2 (Fig. 3F-H, right
233 traces). Fitting single exponential functions to these traces reveals rates of 0.59 ± 0.003 and
234 7.34 ± 0.1 s^{-1} at 1 and 10 μM ATP, respectively (Fig. 3K). At 1000 μM ATP, the observed rate
235 (> 187 s^{-1}) was limited by the size of the covariance smoothing window (5.25 ms; Fig. 3K).
236 The observed rates at 1 and 10 μM ATP are consistent with the second order rate constant
237 for ATP binding of 0.39 ± 0.017 $\mu M^{-1}s^{-1}$ measured by stopped-flow kinetics (K_1'k_{+2}',
238 Table 1).

239 We determined the detachment rates of actomyosin events by plotting the
240 cumulative frequency of individual attachment durations and fitting a single exponential
241 function to the data by maximum likelihood estimation (Fig. 3I). Data from 1 and 10 μM
242 ATP were well fit by single exponentials with rates of 0.88 and 6.87 s^{-1}, respectively (Fig. 3I,

243 Fig. 3K). These rates match well with the observed rate of ATP binding (Table 1), as well as
244 the fits for the reverse ensemble averages, indicating that at sub-saturating ATP (1 and 10
245 μM), detachment is limited by ATP binding (Figure 3J, blue squares & gray diamonds, Fig.
246 3K). Data from 1000 μM ATP were best described as the sum of 2 exponentials, with the
247 major rate of 67.8 s^{-1} comprising 92.1% of the total, and a minor rate of 11.6 s^{-1} comprising
248 7.9% of the total (Fig. 3I, Fig. 3K). The major rate is consistent with both the observed ADP
249 release rate and the measured forward ensemble average rates, indicating that at
250 saturating ATP, ADP release limits detachment of actomyosin interactions (Fig. 3J**,** blue
251 square and black diamond, Fig. 3K).
252

253 **Myo5 is a relatively force-insensitive motor**

254 To elucidate the force sensitivity of Myo5, we measured how its actin detachment rate was
255 affected by mechanical force opposing the power stroke using an isometric feedback
256 system that maintained the actin filament near its initial position (Takagi et al., 2006). The
257 initial force applied to Myo5 in this system depends in part on where along the actin
258 filament Myo5 stochastically binds, so this approach allowed measurement of attachment
259 durations at a range of resistive forces (Fig. 4A). Plotting attachment durations as a
260 function of force revealed a general trend of longer attachment durations at higher
261 resisting forces. At each interaction force, attachment durations are exponentially
262 distributed and, as expected based on prior isometric feedback experiments, the data
263 appear noisy when plotted this way (Fig. 4A). Converting these data to detachment rates by
264 binning them by force at every ten points, averaging, and taking the inverse of the
265 attachment duration more clearly reveals the trend (Fig. 4B).

266 The force dependence of the Myo5 detachment rate was fit by the Bell Equation:

267 $$k(F) = k_0 \cdot e^{\frac{-F \cdot d}{k_B \cdot T}}$$ (**Equation 4**)

268 where *k(F)* is the detachment rate at force *F*, k_0 is the detachment rate in the absence of
269 load, *d* is the distance parameter (the distance to the force-dependent transition state and a
270 measure of force sensitivity), k_B is Boltzmann's constant, and *T* is the temperature. Best fit
271 parameters for k_0 and *d* were determined by maximum likelihood estimation of the
272 unaveraged data from Fig. 4A, incorporating the instrument response time (15-30 ms,
273 Woody et al., 2016). The estimated detachment rate in the absence of force is 67.6 s^{-1}, in
274 close agreement with the measured detachment rate under low load conditions at 1000 μM
275 (saturating) ATP (67.8 s^{-1}, Fig. 3K). The best fit value for the distance parameter, *d*, was
276 1.14 nm.

277 To put Myo5's force sensitivity in context, we re-plotted the function describing the
278 force-dependent actin detachment rate of Myo5 alongside the same curves for vertebrate
279 Myo1b, Myo1c, and β-cardiac myosin, which have previously been determined by the same
280 experimental approach (Fig. 4C, Laakso et al., 2010; Greenberg et al., 2012; Woody et al.,
281 2018). The mechanochemistry of Myo5 (*d* = 1.14 nm) is most like that of β-cardiac (muscle)
282 myosin (*d* = 1.3 nm), suggesting that it is well-suited for generating power. The difference
283 between Myo5 and acutely force-sensitive Myo1b, a tension-sensitive anchor myosin (*d* =
284 15 nm), is dramatic. From 0 to 2 pN of resistance, Myo1b attachment lifetimes slow from
285 ~600 ms to ~45 s, resulting in negligible power generation (Fig. 4D). Over the same
286 interval, Myo5 attachment lifetimes slow very modestly from ~15 ms to ~25 ms, allowing

287 it to generate considerable power (Fig. 4D). Thus, Myo5 is unlikely to act as a force-
288 sensitive anchor in cells and is more likely to power movements against a resisting load.
289

290 **Proposed function of type I myosin in clathrin-mediated endocytosis**

291 Myo5 is one of the best-studied myosin-1 proteins in vivo. Quantitative live cell imaging
292 and electron microscopy have revealed that it is recruited to CME sites simultaneously with
293 initiation of actin assembly, where it concentrates at the base of the site as membrane
294 invagination proceeds (Jonsdottir and Li, 2004; Idrissi et al., 2008). Although it has long
295 been appreciated that the presence (Geli and Riezman, 1996; Goodson et al., 1996) and
296 mechanochemical activity (Sun et al., 2006) of type-1 myosins are required for CME, the
297 mechanistic contribution of motor activity to the dynamic actin network was unknown.
298 When it was discovered that some type I myosins are acutely force sensitive (Laakso et al.,
299 2008), it became apparent that these motors could have mechanochemical activities that
300 range from force-dependent anchoring to power generation during CME. However,
301 distinguishing among these possibilities has been difficult in cells. Mutant Myo5 molecules
302 lacking the motor head or bearing mutations intended to lock the ATPase in low and high
303 actin affinity states each block CME, results that do not reveal the mechanochemical role of
304 Myo5 (Lewellyn et al., 2015; Idrissi et al., 2012). Perhaps the most informative finding in
305 cells has been the observation that varying the number of type I myosins at CME sites
306 results in differences in actin assembly rates (Manenschijn et al., 2019). However, because
307 resistive load remodels growing branched actin networks in complex ways (Bieling et al.,
308 2016), even this finding did not clearly differentiate between the possible roles for
309 endocytic myosin-1s.

310 Here we have shown that Myo5's motor generates power rather than forming force-
311 sensitive catch bonds. The overall ATPase rate of Myo5 is slow relative to other power-
312 generating myosins, but its power stroke and detachment from actin are fast, and they slow
313 only modestly under load (Fig. 4C). Myo5's relative force insensitivity means it generates
314 steady power against resistance (Fig. 4D). Because Myo3 and Myo5 can each support CME
315 in the absence of the other, we suspect that Myo3 is similarly force-insensitive. Given the
316 structural and functional homology between Myo5 and vertebrate Myo1e, together with
317 the close agreement of their unloaded kinetics (El Mezgueldi et al., 2002), we also predict
318 the Myo1e generates biologically relevant power.
319 Our finding that Myo5's kinetics are relatively force insensitive lead us to interpret
320 the previously described dose dependence of actin assembly on the number of myosin-1s
321 at endocytic sites to mean that this motor moves actin filaments at CME sites to power
322 plasma membrane invagination and create space for new monomers to assemble
323 (Manenschijn et al., 2019, Fig. 1, right). On the order of 300 myosin molecules (Myo3 and
324 Myo5 combined) are present at CME sites, mostly where the invaginating membrane meets
325 the plasma membrane (Mund et al., 2018; Idrissi et al., 2008; Sun et al., 2019; Picco et al.,
326 2015). A related myosin, Myo1c, also binds membranes and can generate and sustain sub-
327 piconewton forces parallel to the plane of the membrane, and greater forces when moving
328 actin filaments away from the membrane or when diffusion within the bilayer is impeded
329 (Pyrpassopoulos et al., 2016). Myo5's diffusion is likely to be impeded by the many proteins
330 at the base of CME sites, and it may move actin filaments at an angle to the membrane it is
331 bound to. Actin subunits "treadmill" towards the cytoplasm in endocytic actin networks at
332 ~50-100 nm/s (Kaksonen et al., 2005, 2003), so Myo5's motility rate of 700-900 nm/s (Fig.

333 2G), which we would expect resistance to slow only modestly, is fast enough to do work on
334 the actin network as it assembles. We therefore expect that the myosins power membrane
335 invagination and relive load to accelerate actin assembly during CME.

336 Type I myosins are involved in a variety of membrane reshaping events in cells,
337 where they often interact with growing branched actin networks (Sokac et al., 2006;
338 Almeida et al., 2011; Joensuu et al., 2014; Krendel et al., 2007; Cheng et al., 2012), but the
339 relative contributions of myosin motor activity and actin assembly have rarely been
340 resolved. Here, we demonstrated that a type I myosin critical for CME, a process well-
341 known to be driven by actin assembly, generates power. Implication of endocytic type I
342 myosin as a force-insensitive motor suggests that actin assembly and myosin power
343 generation can be coordinated to do coherent work in membrane remodeling processes.

344 **Materials and methods**

345

346 **Reagents, proteins, and buffers**

347 ATP concentrations were determined spectrophotometrically after each experiment by
348 absorbance at 259 nm, $\epsilon_{259} = 15{,}400\ M^{-1}cm^{-1}$. Rabbit skeletal muscle actin was prepared
349 and gel filtered (Spudich and Watt, 1971). Actin concentrations were determined
350 spectrophotometrically by absorbance at 290 nm, $\epsilon_{290} = 26{,}600\ M^{-1}cm^{-1}$. All actin was
351 stabilized with one molar equivalent of phalloidin (Sigma). Steady state, transient, and
352 single molecule experiments were performed at 20°C in KMg25 buffer (60 mM MOPS pH 7,
353 25 mM KCl, 1 mM EGTA, 1 mM $MgCl_2$, 1 mM DTT). Apyrase VII was obtained from Sigma.
354 Purity and concentration of purified proteins were determined by comparing in-gel
355 Coomassie blue staining to staining of known amounts of bovine serum albumin (Pierce).

356

357 **Expression and Purification of Cmd1**

358 The *S. cerevisiae* calmodulin gene *CMD1* was cloned from genomic DNA into a bacterial
359 expression plasmid with a sequence encoding His_6-TEV situated at the 5' end to generate
360 pDD2743. pDD2743 was transformed into Rosetta *E. coli*, optimized for expression
361 (Novagen). A saturated overnight culture in LB (10 g/L Bacto tryptone, 5 g/L Bacto yeast
362 extract, 10 g/L NaCl) was used to inoculate a 1 L culture in LB to $OD_{600} = 0.1$. Cells were
363 grown to $OD_{600} = 0.6$-1, induced with 0.5 mM IPTG for 5 hours at 37°C, pelleted at 4,225 x g
364 for 20 minutes at 4°C in a Sorvall SLA-3000 (fixed angle) rotor, washed with cold 20 mM
365 HEPES pH 7.5, and repelleted at 2,250 x g for 10 minutes at 4°C in a Jouan CR3i (swinging
366 bucket) centrifuge. Cell pellets were flash frozen in 45 mL lysis buffer (20 mM HEPES pH

367 7.5, 1 M KCl, 20 mM Imidazole). Upon thawing, cells were lysed by sonication, 2 mg DNase I
368 (Roche) and triton X-100 to 1% were added, and the resulting lysate was incubated on ice
369 for 30 minutes, then spun at 92,000 x g for 25 minutes in a Beckman Type 70 Ti rotor. The
370 supernatant was loaded onto a 1 mL HisTrap HP column (GE healthcare) preequilibrated
371 with binding buffer (20 mM HEPES pH 7.5, 500 mM KCl, 20 mM imidazole). The column
372 was washed with 20 mL binding buffer, and Cmd1 was eluted using a 30 mL linear gradient
373 from 0-100% elution buffer (20 mM HEPES pH 7.5, 500 mM KCl, 500 mM imidazole).
374 Fractions containing Cmd1 were pooled, Cmd1 was cleaved from His_6 with TEV protease
375 and dialyzed overnight at 4°C into low salt buffer (10 mM Tris pH 7, 25 mM NaCl, 2 mM
376 $MgCl_2$, 5 mM DTT). Following dialysis, purified, cleaved Cmd1 was bound to a MonoQ
377 column and eluted using a 10 mL linear gradient from 0-70% high salt buffer (10 mM Tris
378 pH 7, 1 M NaCl, 2 mM $MgCl_2$, 5 mM DTT). Fractions containing Cmd1 were pooled, dialyzed
379 into KMg50 buffer (60 mM MOPS pH 7, 50 mM KCl, 1 mM $MgCl_2$, 1 mM EGTA, 1 mM DTT,
380 5% glycerol), and stored at -80°C.
381

382 **Expression and Purification of Myo5**

383 Myo5 was coexpressed with the myosin chaperone She4 in *S. cerevisiae.* The *MYO5* open
384 reading frame (ORF) from *S. cerevisiae* was cloned from genomic DNA and truncated at
385 Gly^{763}, generating a construct containing the motor domain and both Cmd1-binding IQ
386 motifs of the lever arm. The *SHE4* ORF was cloned in its entirety from *S. cerevisiae* genomic
387 DNA. Both ORFs were ligated into a 2μ expression plasmid with a partially defective *LEU2*
388 gene (*leu2d*) to ensure high copy number, creating plasmid pDD2744 (parent vector
389 described in Roy et al., 2011). The *MYO5* ORF was situated with a sequence encoding

390 AviTag-TEV-His_9 at the 3' end. Expression of the *MYO5* and *SHE4* ORFs was driven by a
391 bidirectional Gal 1/10 promotor.
392 pDD2744 was transformed into D1074 yeast (Roy et al., 2011). Saturated overnight
393 cultures in synthetic minimal medium (1.5 g/L Difacto yeast nitrogen base, 5 g/L
394 ammonium sulfate, supplemented with 2% glucose 20 µg/mL adenine, L-histadine, L-
395 methionine, and 30 µg/mL L-lysine) were used to inoculate 1.5 L cultures in the same
396 media with raffinose substituted for glucose to OD_{600} = 0.1. After 18 hours of growth at
397 30°C, cultures were induced with 2% galactose, Bacto yeast extract was added to 10 g/L,
398 and Bacto peptone to 20 g/L. After 8 hours of expression, the cells were harvested at 4,225
399 x g for 20 minutes at 4°C in a Sorvall SLA-3000 rotor, washed with 25 mL cold Milli-Q
400 water, repelleted at 2,250 x g for 10 minutes at 4°C in a Jouan CR3i centrifuge, resuspended
401 in 0.2 volumes of cold Milli-Q water, and drop frozen into liquid nitrogen. Lysis was
402 achieved through cryomilling (10 cycles of 3 minutes grinding with one minute cooldown)
403 in the large vials of a 6870 freezer/mill (SPEX Sample Prep).
404 Cell powders were thawed in binding buffer (10 mM Tris pH 7, 500 mM NaCl, 4 mM
405 $MgCl_2$, 2 mM ATP, 20 mM imidazole, 5 mM DTT) supplemented with 1 mM PMSF, 1 x
406 cOmplete protease inhibitor cocktail without EDTA (Roche), and 1 µM Cmd1. For
407 purification of phosphorylated Myo5, 1 µg Pak1 (Sigma, Brzeska et al., 1997, Fig. S1) was
408 included in the lysis buffer and 10 mM β-glycerophosphate, 5 mM sodium pyrophosphate,
409 and 50 mM sodium fluoride were included in all purification buffers. For purification of
410 unphosphorylated Myo5, 4000 units lambda phosphatase (NEB) and 1 mM $MnCl_2$ were
411 included in the lysis buffer. The lysate was then spun at 345,000 x g for 10 minutes at 4°C
412 in a Beckman TLA100.3 rotor, filtered through a 0.22 µm filter, and loaded onto a 1 mL

413 HisTrap HP column. The column was washed with wash buffer (Binding buffer with only
414 200 mM NaCl), and Myo5 was eluted using a 20 mL linear gradient from 0-100% elution
415 buffer (wash buffer with 1 M imidazole).

416 Fractions containing Myo5 were pooled and supplemented with Cmd1 to 1 μM. For
417 unphosphorylated Myo5 purification, a further 20,000 units lambda phosphatase were
418 added along with $MnCl_2$ to 1 mM and the fractions were incubated at 30°C for 30 minutes.
419 Purified protein was dialyzed through a 3.5 KDa MWCO membrane into 1 L storage buffer
420 (KMg50 with 50% glycerol) overnight at 4°C and again into 500 mL of the same buffer for 2
421 hours at 4°C, then stored at -20°C.

422

423 **Kinetic measurements**

424 Kinetic experiments were conducted using an Applied Photophysics (Surrey, UK) SX.18 MV
425 stopped-flow apparatus. To monitor light scattering at 90˚, 450 nm excitation light was
426 used with a 400 nm emission filter. Experimental transients were fit by single exponentials
427 using the software provided with the stopped flow apparatus. 1-7 traces were averaged
428 together to generate each data point. Steady state actin-activated ATPase activity was
429 measured using the NADH enzyme-linked assay (De La Cruz and Ostap, 2009). NADH loss
430 was monitored by absorbance at 340 nm (ϵ_{340} = 6,220 $M^{-1}cm^{-1}$). ATP-induced dissociation
431 of actoMyo5 was measured and analyzed as described (De La Cruz and Ostap, 2009). 0.04
432 units/mL apyrase was added to solutions of actoMyo5 before mixing to remove
433 contaminating ADP and ATP. Unphosphorylated actoMyo5 required prolonged treatment
434 with apyrase to achieve sufficient signal, presumably because a larger fraction of the

435 population was bound to ATP left over from purification and because the actin-activated
436 ATPase rate of unphosphorylated Myo5 is slow. Concentrations reported are post mixing.
437

438 **Motility assays**

439 Motility assays were performed essentially as described (Lin et al., 2005). Myo5 was
440 adhered to nitrocellulose coated coverslips via 20 μg anti His_6 antibody (Sigma) blocked
441 with 2 mg/mL casein. Blocking coverslips with bovine serum albumin (BSA) led to inferior
442 gliding. Motility was recorded in the presence of 1 mM ATP and 5 μM Cmd1. The rate of
443 actin filament gliding was determined using the manual tracking plugin in Fiji.
444

445 **Optical trapping**

446 Flow chambers for optical trapping were constructed with double-sided tape and vacuum
447 grease as previously described (Snoberger et al., 2021; Greenberg et al., 2017). Briefly, the
448 coverslip was coated with a 0.1% mixture of nitrocellulose and 2.47 μm diameter silica
449 beads. Coverslips were dried at least 30 minutes and were used within 24 hours of
450 preparation. To define the walls of the flow cell, 2 strips of double-sided tape were placed
451 ~5 mm apart, a 1 mm thick glass slide was placed on top, and carefully sealed with vacuum
452 grease after addition of final buffer.
453 Trapping buffer (KMg25 with 1 mM DTT freshly added) was used for all trapping
454 assays. A 100x stock of glucose oxidase + catalase (GOC) was freshly prepared by
455 centrifuging catalase (Sigma, > 30000 $U \cdot mL^{-1}$) at 15,000 x g for 1 minute, and adding 2 μl of
456 catalase supernatant to 20 μL of 19.1 U/μL glucose oxidase (Sigma).

457 0.01 mg/mL anti-His_6 antibody (Sigma) was flowed in the chamber and incubated
458 between 30 seconds and 3 minutes, then immediately blocked with two, 3-minute
459 incubations of 1 - 2 mg/mL BSA. Stocks of phosphorylated His_9-tagged Myo5 were diluted
460 to 1 nM in trapping buffer with 300 mM added KCl and incubated in the flow cell for 2
461 minutes. The number of myosins bound to the surface was limited by the surface
462 concentration of anti-His_6 antibody, and the incubation time of anti-His_6 antibody was
463 adjusted daily between 30 seconds and 3 minutes such that 1 of 3 - 5 pedestals tested
464 showed clear myosin interactions with the actin dumbbell.
465 Following incubation with Myo5, a second blocking step with two, 3-minute
466 incubations of 1 - 2 mg/mL BSA was performed. Final buffer added to the flow cell
467 contained trapping buffer with indicated amount of ATP, 1 μL of GOC added immediately
468 prior to addition to chamber, and 0.1 - 0.25 nM rabbit skeletal muscle actin polymerized
469 with 15% biotinylated actin (Cytoskeleton) stabilized by rhodamine-phalloidin (Sigma) at a
470 1.1-1.2 molar ratio with G-actin concentration. Neutravidin-coated beads were prepared by
471 incubating 0.4 ng of 0.8 μm diameter polystyrene beads (Polysciences) and coated with 5
472 mg/mL neutravidin (Thermo Fisher). 3 μL of neutravidin-coated beads were added to one
473 side of the chamber prior to sealing. All trapping data were acquired within 90 minutes of
474 addition of the final buffer to the chamber.
475 Optical trapping experiments were performed at room temperature (20 ± 1 °C)
476 using a dual beam 1064 nm trapping laser as described in (Woody et al., 2018, 2017). A
477 single laser beam was split into 2 beams using polarizing beam splitters and steered into a
478 60x water immersion objective (Nikon). Laser light was projected through an oil
479 immersion condenser and into quadrant photodiodes (JQ-50P, Electro Optical Components,

480 Inc.), each of which were conjugate to the back focal plane of the objective. Direct force
481 detection from the quadrant photodiodes was achieved using a custom-built high-voltage
482 reverse bias and an amplifier. Data acquisition, beam position control output, and isometric
483 feedback calculations were controlled with custom-built virtual instruments (Labview,
484 Matlab).

485 Individual 0.8 μm diameter neutravidin-coated bead were caught in the two traps
486 and held approximately 5 μm apart. Trap stiffnesses were adjusted to 0.05 – 0.1 pN/nm for
487 each trap. A biotinylated actin filament visualized by rhodamine phalloidin was bound to
488 the two trapped beads, creating a bead-actin-bead dumbbell. The dumbbell was
489 pretensioned (3-5 pN) by steering one beam using a piezo controlled mirror conjugate to
490 the back focal plane of the objective, and the surface of pedestal beads were probed for
491 myosins. Putative myosin interactions were detected via drops in variance of the two
492 beads, and the 3-dimensional position of the dumbbell relative to the myosin was refined
493 further by maximizing the rate and size of the observed power stroke deflections. Every 30-
494 60 s, the dumbbell was moved axially along the actin filament in ~6 nm steps between
495 trace acquisition to ensure even accessibility of actin-attachment target zones. Stage drift
496 was corrected via a feedback system using a nano-positioning stage and imaging the
497 position of the pedestal bead with nm precision (Woody et al., 2017). In experiments using
498 1 μM ATP, due to the longer actomyosin interactions, stage drift was still observed even
499 with the stage feedback engaged, leading to a presumed underestimation of the
500 displacement size. All data were acquired at a sampling rate of 250 kHz.

501 Isometric optical clamping experiments were performed as described in (Woody et
502 al., 2018; Takagi et al., 2006) using a digital feedback loop and a 1-D electro-optical

503 deflector (EOD, LTA4-Crystal, Conoptics) to steer the beam position using input from a high
504 voltage source (Conoptics, Model 420 Amplifier). Briefly, the position of one bead (the
505 "transducer" bead) was maintained at a constant position by adjusting the position of the
506 other bead (referred to as the "motor" bead) during actomyosin interactions. The response
507 time of the feedback loop during actomyosin interactions was ~15-30 ms.
508

509 **Optical trap data analysis**

510 Actomyosin interactions for non-isometric optical clamping experiments were detected
511 using the single-molecule computational tool SPASM (Software for Precise Analysis of
512 Single Molecules , Blackwell et al., 2021), which uses a calculation of the dumbbell bead
513 covariances and a change-point algorithm. Data collected at 1000 μM ATP were analyzed at
514 250 kHz, while data collected at 1 and 10 μM ATP were downsampled to 2 kHz by
515 averaging every 125 points to enhance analysis speed. Events were detected by calculating
516 the covariance of the 2 beads using a smoothing window of 33.3, 15, and 5.25 ms and an
517 averaging window 60, 36, and 12 ms at 1, 10, and 1000 μM ATP, respectively. The
518 instrument deadtime was calculated to be 2 times the covariance averaging window. For
519 each 15 s trace, the detected covariance was plotted and fit to double gaussian
520 distributions, with the smaller mean gaussian corresponding to the actomyosin "bound"
521 portion and the larger mean gaussian corresponding to the "unbound" portion of events. A
522 putative event was defined as an event where the covariance starts above the unbound
523 peak mean, drops below the bound peak mean, and remains below the unbound peak mean
524 for at least the length of the instrument deadtime prior to returning back above unbound
525 peak mean. Event starts and ends were further refined using a changepoint algorithm as

526 described (Blackwell et al., 2021). Attachment durations and ensemble averages of single
527 events were determined using built-in features in the SPASM software. Exponential fits for
528 forward and reverse ensemble averages were performed in Origin 2019 graphing &
529 analysis software (OriginLab).

530 Events detected in isometric optical clamping experiments were detected as
531 described in (Takagi et al., 2006) using a zero crossing analysis via custom MATLAB scripts.
532 Briefly, when a myosin is actively engaged with the dumbbell, force is applied to the
533 transducer bead, a feedback loop is engaged and opposing force applied to the motor bead
534 until the position of the transducer bead is restored. Beginnings of events are defined at the
535 point at which the feedback signal increases from baseline in the motor bead and ends of
536 events are defined when the feedback signal decreases back below the baseline in the
537 motor bead.

538

539 **Online supplemental material**

540 Figure S1 shows the results of a kinase assay demonstrating that Pak1, used to in
541 purifications of phosphorylated Myo5, specifically phosphorylates Myo5 serine-357.

542 **Acknowledgements**

543

544 We thank M. Greenberg, E. Lewellyn, and A. Kunibe, each of whom played important roles
545 at the inception of this study. We thank Y.E. Goldman for optical trap instrumentation. We
546 thank M. Ferrin for helpful comments on the manuscript. This work was funded by National
547 Institute of General Medical Sciences (NIGMS) grant R35 GM118149 to D.G.D and grant
548 5R37GM057247 to E.M.O. R.T.A.P. is currently funded by NIGMS F32 GM142145.

549 **References**

550

551 Aghamohammadzadeh, S., and K.R. Ayscough. 2009. Differential requirements for actin
552 during yeast and mammalian endocytosis. *Nat. Cell Biol.* 11:1039–1042.
553 doi:10.1038/ncb1918.
554 Akamatsu, M., R. Vasan, D. Serwas, M. Ferrin, P. Rangamani, and D.G. Drubin. 2020.
555 Principles of self-organization and load adaptation by the actin cytoskeleton during
556 clathrin-mediated endocytosis. *Elife*. 9:1–40. doi:10.7554/eLife.49840.
557 Almeida, C.G., A. Yamada, D. Tenza, D. Louvard, G. Raposo, and E. Coudrier. 2011. Myosin 1b
558 promotes the formation of post-Golgi carriers by regulating actin assembly and
559 membrane remodelling at the trans-Golgi network. *Nat. Cell Biol.* 13:779–789.
560 doi:10.1038/ncb2262.
561 Basu, R., E.L. Munteanu, and F. Chang. 2013. Role of turgor pressure in endocytosis in
562 fission yeast. *Mol. Biol. Cell*. 25:679–87. doi:10.1091/mbc.E13-10-0618.
563 Bement, W.M., and M.S. Mooseker. 1995. TEDS rule: A molecular rationale for differential
564 regulation of myosins by phosphorylation of the heavy chain head. *Cell Motil.*
565 *Cytoskeleton*. 31:87–92. doi:10.1002/cm.970310202.
566 Bieling, P., T. Li, J. Weichsel, R. Mcgorty, P. Jreij, B. Huang, D.A. Fletcher, and R.D. Mullins.
567 2016. Force Feedback Controls Motor Activity and Mechanical Properties of Self-
568 Assembling Branched Actin Networks. *Cell*. 164:115–127.
569 doi:10.1016/j.cell.2015.11.057.
570 Blackwell, T., W.T. Stump, S.R. Clippinger, and M.J. Greenberg. 2021. Computational Tool for
571 Ensemble Averaging of Single-Molecule Data. *Biophys. J.* 120:10–20.

572 doi:10.1016/j.bpj.2020.10.047.
573 Boulant, S., C. Kural, J.-C. Zeeh, F. Ubelmann, and T. Kirchhausen. 2011. Actin dynamics
574 counteract membrane tension during clathrin-mediated endocytosis. *Nat. Cell Biol.*
575 13:1124–31. doi:10.1038/ncb2307.
576 Brzeska, H., U.G. Knaus, Z.Y. Wang, G.M. Bokoch, and E.D. Korn. 1997. p21-activated kinase
577 has substrate specificity similar to Acanthamoeba myosin I heavy chain kinase and
578 activates Acanthamoeba myosin I. *Proc. Natl. Acad. Sci. U. S. A.* 94:1092–1095.
579 Busch, D.J., J.R. Houser, C.C. Hayden, M.B. Sherman, E.M. Lafer, and J.C. Stachowiak. 2015.
580 Intrinsically disordered proteins drive membrane curvature. *Nat. Commun.* 6.
581 doi:10.1038/ncomms8875.
582 Cail, R.C., C.R. Shirazinejad, and D.G. Drubin. 2022. Induced nanoscale membrane curvature
583 bypasses the essential endocytic function of clathrin. *J. Cell Biol.* 221.
584 doi:10.1083/jcb.202109013.
585 Carlsson, A.E. 2018. Membrane bending by actin polymerization. *Curr. Opin. Cell Biol.* 50:1–
586 7. doi:10.1016/j.ceb.2017.11.007.
587 Chen, C., M.J. Greenberg, J.M. Laakso, E.M. Ostap, Y.E. Goldman, and H. Shuman. 2012.
588 Kinetic schemes for post-synchronized single molecule dynamics. *Biophys. J.* 102.
589 doi:10.1016/j.bpj.2012.01.054.
590 Cheng, J., A. Grassart, and D.G. Drubin. 2012. Myosin 1E coordinates actin assembly and
591 cargo trafficking during clathrin-mediated endocytosis. *Mol. Biol. Cell*. 23:2891–904.
592 doi:10.1091/mbc.E11-04-0383.
593 Dannhauser, P.N., and E.J. Ungewickell. 2012. Reconstitution of clathrin-coated bud and
594 vesicle formation with minimal components. *Nat. Cell Biol.* 14:634–639.

595 doi:10.1038/ncb2478.
596 Evangelista, M., B.M. Klebl, A.H. Yong, B.A. Webb, T. Leeuw, E. Leberer, M. Whiteway, D.Y.
597 Thomas, and C. Boone. 2000. A Role for Myosin-I in Actin Assembly through
598 Interactions with Vrp1p, Bee1p, and the Arp2/3 Complex. *J. Cell Biol.* 148:353–362.
599 doi:10.1083/jcb.148.2.353.
600 Geli, M.I., and H. Riezman. 1996. Role of Type I Myosins in Receptor-Mediated Endocytosis
601 in Yeast. *Science*. 272:533–535.
602 Geli, M.I., A. Wesp, and H. Riezman. 1998. Distinct functions of calmodulin are required for
603 the uptake step of receptor-mediated endocytosis in yeast: The type I myosin Myo5p is
604 one of the calmodulin targets. *EMBO J.* 17:635–647. doi:10.1093/emboj/17.3.635.
605 Goodson, H. V, B.L. Anderson, H.M. Warrick, L.A. Pon, and J.A. Spudich. 1996. Synthetic
606 lethality screen identifies a novel yeast myosin I gene (MYO5): myosin I proteins are
607 required for polarization of the actin cytoskeleton. *J. Cell Biol.* 133:1277–1291.
608 doi:10.1083/JCB.133.6.1277.
609 Greenberg, M.J., T. Lin, Y.E. Goldman, H. Shuman, and E.M. Ostap. 2012. Myosin IC generates
610 power over a range of loads via a new tension-sensing mechanism. *Proc. Natl. Acad.*
611 *Sci. U. S. A.* 109:E2433-40. doi:10.1073/pnas.1207811109.
612 Greenberg, M.J., and E.M. Ostap. 2013. Regulation and control of myosin-I by the motor and
613 light chain-binding domains. *Trends Cell Biol.* 23:81–9. doi:10.1016/j.tcb.2012.10.008.
614 Greenberg, M.J., H. Shuman, and E.M. Ostap. 2017. Measuring the Kinetic and Mechanical
615 Properties of Non-processive Myosins Using Optical Tweezers. *Methods Mol. Biol.*
616 1486:483–509. doi:10.1201/b22505.
617 Grosshans, B.L., H. Grötsch, D. Mukhopadhyay, I.M. Fernández, J. Pfannstiel, F.-Z. Idrissi, J.

618 Lechner, H. Riezman, and M.I. Geli. 2006. TEDS site phosphorylation of the yeast
619 myosins I is required for ligand-induced but not for constitutive endocytosis of the G
620 protein-coupled receptor Ste2p. *J. Biol. Chem.* 281:11104–14.
621 doi:10.1074/jbc.M508933200.
622 Hassinger, J.E., G. Oster, D.G. Drubin, and P. Rangamani. 2017. Design principles for robust
623 vesiculation in clathrin-mediated endocytosis. *Proc. Natl. Acad. Sci. U. S. A.* 114:E1118–
624 E1127. doi:10.1073/pnas.1617705114.
625 Idrissi, F.-Z., A. Blasco, A. Espinal, and M.I. Geli. 2012. Ultrastructural dynamics of proteins
626 involved in endocytic budding. *Proc. Natl. Acad. Sci. U. S. A.* 109:E2587–E2594.
627 doi:10.1073/pnas.1202789109.
628 Idrissi, F.Z., H. Grötsch, I.M. Fernández-Golbano, C. Presciatto-Baschong, H. Riezman, and
629 M.I. Geli. 2008. Distinct acto/myosin-I structures associate with endocytic profiles at
630 the plasma membrane. *J. Cell Biol.* 180:1219–1232. doi:10.1083/jcb.200708060.
631 Joensuu, M., I. Belevich, O. Rämö, I. Nevzorov, H. Vihinen, M. Puhka, T.M. Witkos, M. Lowe,
632 M.K. Vartiainen, and E. Jokitalo. 2014. ER sheet persistence is coupled to myosin 1c-
633 regulated dynamic actin filament arrays. *Mol. Biol. Cell*. 25:1111–1126.
634 doi:10.1091/mbc.E13-12-0712.
635 Jonsdottir, G. a., and R. Li. 2004. Dynamics of Yeast Myosin I: Evidence for a Possible Role in
636 Scission of Endocytic Vesicles. *Development*. 14:1604–1609. doi:10.1016/j.
637 Jontes, J.D., E.M. Wilson-Kubalek, and R.A. Milligan. 1995. A 32 degree tail swing in brush
638 border myosin I on ADP release. *Nature*. 378:751–753. doi:10.1038/378751a0.
639 Kaksonen, M., Y. Sun, and D.G. Drubin. 2003. A pathway for association of receptors,
640 adaptors, and actin during endocytic internalization. *Cell*. 115:475–87.

641 Kaksonen, M., C.P. Toret, and D.G. Drubin. 2005. A modular design for the clathrin- and
642 actin-mediated endocytosis machinery. *Cell*. 123:305–20.
643 doi:10.1016/j.cell.2005.09.024.
644 Kaplan, C., S.J. Kenny, X. Chen, J. Schöneberg, E. Sitarska, A. Diz-Muñoz, M. Akamatsu, K. Xu,
645 and D.G. Drubin. 2022. Load adaptation by endocytic actin networks. *Mol. Biol. Cell*. 33.
646 doi:10.1091/mbc.E21-11-0589.
647 Krendel, M., E.K. Osterweil, and M.S. Mooseker. 2007. Myosin 1E interacts with
648 synaptojanin-1 and dynamin and is involved in endocytosis. *FEBS Lett.* 581:644–50.
649 doi:10.1016/j.febslet.2007.01.021.
650 De La Cruz, E.M., and E.M. Ostap. 2009. Kinetic and Equilibrium Analysis of the Myosin
651 ATPase. *Methods Enzymol.* 455:157–192. doi:10.1016/S0076-6879(08)04206-7.
652 Laakso, J.M., J.H. Lewis, H. Shuman, and E.M. Ostap. 2008. Myosin I can act as a molecular
653 force sensor. *Science*. 321:133–6. doi:10.1126/science.1159419.
654 Laakso, J.M., J.H. Lewis, H. Shuman, and E.M. Ostap. 2010. Control of myosin-I force sensing
655 by alternative splicing. *Proc. Natl. Acad. Sci. U. S. A.* 107:698–702.
656 doi:10.1073/pnas.0911426107.
657 Lewellyn, E.B., R.T. Pedersen, J. Hong, R. Lu, H.M. Morrison, and D.G. Drubin. 2015. An
658 Engineered Minimal WASP-Myosin Fusion Protein Reveals Essential Functions for
659 Endocytosis. *Dev. Cell*. 35:281–294. doi:10.1016/j.devcel.2015.10.007.
660 Lewis, J.H., T. Lin, D.E. Hokanson, and E.M. Ostap. 2006. Temperature dependence of
661 nucleotide association and kinetic characterization of Myo1b. *Biochemistry*. 45:11589–
662 97. doi:10.1021/bi0611917.
663 Lin, T., N. Tang, and E.M. Ostap. 2005. Biochemical and motile properties of Myo1b splice

664 isoforms. *J. Biol. Chem.* 280:41562–41567. doi:10.1074/jbc.M508653200.

665 Manenschijn, H.E., A. Picco, M. Mund, J. Ries, and M. Kaksonen. 2019. Type-I myosins
666 promote actin polymerization to drive membrane bending in endocytosis. *Elife*.
667 17:490011. doi:10.1101/490011.

668 El Mezgueldi, M., N. Tang, S.S. Rosenfeld, and E.M. Ostap. 2002. The Kinetic Mechanism of
669 Myo1e (Human Myosin-IC). *J. Biol. Chem.* 277. doi:10.1074/jbc.M200713200.

670 Mogilner, A., and G. Oster. 1996. Cell motility driven by actin polymerization. *Biophys. J.*
671 71:3030–3045. doi:10.1016/S0006-3495(96)79496-1.

672 Mogilner, A., and G. Oster. 2003. Force Generation by Actin Polymerization II: The Elastic
673 Ratchet and Tethered Filaments. *Biophys. J.* 84:1591–1605. doi:10.1016/S0006-
674 3495(03)74969-8.

675 Mund, M., J.A. Van Der Beek, J. Deschamps, S. Dmitrieff, P. Hoess, J.L. Monster, A. Picco, F.
676 Nedelec, M. Kaksonen, and J. Ries. 2018. Systematic Nanoscale Analysis of Endocytosis
677 Links Efficient Vesicle Formation to Patterned Actin Nucleation. *Cell*. 174:884–896.
678 doi:10.1016/j.cell.2018.06.032.

679 Nickaeen, M., J. Berro, T.D. Pollard, and B.M. Slepchenko. 2019. Actin assembly produces
680 sufficient forces for endocytosis in yeast. *Mol. Biol. Cell*. 30:2014–2024.
681 doi:10.1091/mbc.E19-01-0059.

682 Pedersen, R.T., and D.G. Drubin. 2019. Type I myosins anchor actin assembly to the plasma
683 membrane during clathrin-mediated endocytosis. *J. Cell Biol.* 218:1138–1147.
684 doi:10.1083/jcb.201810005.

685 Picco, A., M. Mund, J. Ries, F. Nedelec, and M. Kaksonen. 2015. Visualizing the functional
686 architecture of the endocytic machinery. *Elife*. 4:1–29. doi:10.7554/eLife.04535.

687 Pyrpassopoulos, S., G. Arpağ, E.A. Feeser, H. Shuman, E. Tüzel, and E.M. Ostap. 2016. Force
688 generation by membrane-associated myosin-I. *Sci. Rep.* 6:1–14.
689 doi:10.1038/srep25524.
690 Roy, M.A., N. Siddiqui, and D. D'Amours. 2011. Dynamic and selective DNA-binding activity
691 of Smc5, a core component of the Smc5-Smc6 complex. *Cell Cycle*. 10:690–700.
692 doi:10.4161/cc.10.4.14860.
693 Skruzny, M., T. Brach, R. Ciuffa, S. Rybina, M. Wachsmuth, and M. Kaksonen. 2012.
694 Molecular basis for coupling the plasma membrane to the actin cytoskeleton during
695 clathrin-mediated endocytosis. *Proc. Natl. Acad. Sci. U. S. A.* 109:E2533–E2542.
696 doi:10.1073/pnas.1207011109.
697 Snoberger, A., B. Barua, J.L. Atherton, H. Shuman, E. Forgacs, Y.E. Goldman, D.A.
698 Winkelmann, and E.M. Ostap. 2021. Myosin with hypertrophic cardiac mutation r712l
699 has a decreased working stroke which is rescued by omecamtiv mecarbil. *Elife*. 10:1–
700 24. doi:10.7554/eLife.63691.
701 Sokac, A.M., C. Schietroma, C.B. Gundersen, and W.M. Bement. 2006. Myosin-1c couples
702 assembling actin to membranes to drive compensatory endocytosis. *Dev. Cell*. 11:629–
703 40. doi:10.1016/j.devcel.2006.09.002.
704 Spudich, J.A., and S. Watt. 1971. The Regulation of Rabbit Skeletal Muscle Contraction. *J.*
705 *Biol. Chem.* 246:4866–4871.
706 Stewart, T.J., V. Murthy, S.P. Dugan, and J.E. Baker. 2021. Velocity of myosin-based actin
707 sliding depends on attachment and detachment kinetics and reaches a maximum when
708 myosin-binding sites on actin saturate. *J. Biol. Chem.* 297.
709 doi:10.1016/j.jbc.2021.101178.

710 Sun, Y., A.C. Martin, and D.G. Drubin. 2006. Endocytic Internalization in Budding Yeast
711 Requires Coordinated Actin Nucleation and Myosin Motor Activity. *Dev. Cell*. 11:33–46.
712 doi:10.1016/j.devcel.2006.05.008.
713 Sun, Y., J. Schöneberg, X. Chen, T. Jiang, C. Kaplan, K. Xu, T.D. Pollard, and D.G. Drubin. 2019.
714 Direct comparison of clathrin-mediated endocytosis in budding and fission yeast
715 reveals conserved and evolvable features. *Elife*. 8. doi:10.7554/eLife.50749.
716 Takagi, Y., E.E. Homsher, Y.E. Goldman, and H. Shuman. 2006. Force generation in single
717 conventional actomyosin complexes under high dynamic load. *Biophys. J.* 90:1295–
718 1307. doi:10.1529/biophysj.105.068429.
719 Veigel, C., L.M. Coluccio, J.D. Jontes, J.C. Sparrow, R. a Milligan, and J.E. Molloy. 1999. The
720 motor protein myosin-I produces its working stroke in two steps. *Nature*. 398:530–
721 533. doi:10.1038/19104.
722 Woody, M.S., M.J. Greenberg, B. Barua, D.A. Winkelmann, Y.E. Goldman, and E.M. Ostap.
723 2018. Positive cardiac inotrope omecamtiv mecarbil activates muscle despite
724 suppressing the myosin working stroke. *Nat. Commun.* 9. doi:10.1038/s41467-018-
725 06193-2.
726 Woody, M.S., J.H. Lewis, M.J. Greenberg, Y.E. Goldman, and E.M. Ostap. 2016. MEMLET: An
727 Easy-to-Use Tool for Data Fitting and Model Comparison Using Maximum-Likelihood
728 Estimation. *Biophys. J.* 111:273–282. doi:10.1016/j.bpj.2016.06.019.
729 Woody, M.S., E.M. Ostap, Y.E. Goldman, and M. Capitanio. 2017. An ultra-fast EOD-based
730 force-clamp detects rapid biomechanical transitions. SPIE-Intl Soc Optical Eng. 26.
731

732 **Figure 1: Models for the functions of actin assembly and myosin activity during**
733 **membrane deformation for clathrin-mediated endocytosis**
734 Cartoon diagram illustrating the organization of actin filaments and Myo5 molecules at
735 endocytic sites. Actin filaments are bound by coat proteins at the tip of the growing
736 membrane invagination and oriented with their growing ends toward the plasma
737 membrane, powering membrane invagination. The type I myosin Myo5 could either anchor
738 the actin network in a favorable orientation (left) or provide an assisting force (right).
739
740 **Figure 2: In-solution, population biochemical characterization of Myo5**
741 **(A)** Coomassie-stained SDS-polyacrylamide gels showing example preparations of the
742 purified Myo5 motor/lever construct and calmodulin (Cmd1, light chain) used in all
743 experiments. **(B)** The actin concentration dependence of the steady-state ATPase activity of
744 100 nM unphosphorylated (grey circles) and phosphorylated Myo5 (black circles). Each
745 data point represents the average of 6-7 time courses, which were 100 s each. The orange
746 line is a best fit of the phosphorylated Myo5 data to a rectangular hyperbola. **(C)** Schematic
747 pathway for the Myo5 ATPase cycle. Blue motors are in tightly bound conformations, green
748 motors are weakly bound/unbound. **(D)** Example light scattering transients reporting on
749 ATP-induced dissociation of phosphorylated (left, k_{obs} = 17 s^{-1}) and unphosphorylated
750 (right, k_{obs} = 64.1 s^{-1}) actoMyo5, obtained by mixing 100 nM actoMyo5 (AM) with 94 μm
751 and 72 μM ATP, respectively, as shown in the inset schematic. The black line is the fit of a
752 single exponential function to the data. **(E)** ATP concentration dependence of dissociation
753 of 100 nM unphosphorylated (grey circles) and phosphorylated actoMyo5 (black circles).
754 Each data point represents 3-6 time courses averaged and fit to a single exponential decay

755 function. The orange line is a linear best fit of the phosphorylated Myo5 data. The purple
756 line is a best fit of the unphosphorylated Myo5 data to a rectangular hyperbola.
757 **(F)** Example light scattering transients reporting ATP-induced dissociation of ADP-
758 saturated phosphorylated (left) and unphosphorylated (right) actoMyo5, obtained by
759 preincubating 200 nM actoMyo5 (AM) with 100 μM ADP, then mixing rapidly with 2.5 mM
760 ATP, as shown in the inset schematic. The black line is the fit of a single exponential
761 function to the data. **(G)** Velocity of actin filament gliding, measured at varying surface
762 densities of Phospho-Myo5 (black circles, orange line) and unphosphorylated Myo5 (gray
763 circles, purple line) in in vitro motility assays. Myosin concentrations indicate the quantity
764 of protein incubated in the flow chamber before washing. Each data point represents the
765 average velocity of 30 – 60 filaments, and the error bars are standard deviations.
766
767 **Table 1**
768 Summary of rate and equilibrium constants measured for Myo5 in this study. Errors are
769 standard errors of the fits.
770
771 **Figure 3: Single molecule, optical trap analysis of Myo5 step size and kinetics**
772 **(A)** Cartoon schematic of the 3-bead optical trapping setup. A biotinylated actin filament is
773 tethered between two neutravidin-coated beads that are trapped in a dual beam optical
774 trap. This bead-actin-bead "dumbbell" is lowered onto pedestal beads that have been
775 sparsely coated with His_6 antibody to attach Myo5-motor/lever-Avi-Tev-His_9. **(B-D)** Single
776 Myo5 displacements of a single bead position and covariance traces, calculated using both
777 beads, showing single molecule interactions acquired in the presence of 1 μM **(B)** 10 μM

778 **(C)** and 1000 μM ATP. **(D)**. Blue bars indicate attachment events as identified by covariance
779 (gray) decreases. The threshold of event detection by the covariance traces are indicated
780 by dashed gray lines. **(E)** Schematic of displacement traces depicting the 2-step nature of
781 actomyosin displacements in the optical trap. **(F-H)** Binding events were synchronized at
782 their beginnings (left) or ends (right) and averaged forward or backward in time,
783 respectively. Measured total displacement of Myo5 was 5.0 nm at 10 μM ATP, with the 1st
784 substep contributing a 4.8 nm displacement (arrow 1. in G) and the 2nd substep
785 contributing a 0.2 nm displacement (arrow 2. In G). **(F-H, left)** Forward-averaged
786 ensembles synchronized at the beginnings of events. **(F-H, right)** Reverse-averaged
787 ensembles synchronized at the ends of events. Black and gray lines are single exponential
788 fits in the forward and reverse ensembles, respectively. **(I)** Cumulative distributions of
789 attachment durations for Myo5 at 1, 10, and 1000 μM ATP. Blue lines show cumulative
790 frequency of attachment durations at the indicated ATP concentrations, and the red,
791 yellow, and green lines indicate fitted exponential distributions at 1, 10, and 1000 μM ATP,
792 respectively. 1 and 10 μM ATP were fit well to single exponentials, and the 1000 μM ATP
793 data were best described by the sum of two exponentials. **(J)** Summary of rates at 1, 10, and
794 1000 μM ATP calculated from (F-H). Blue boxes are the fitted exponential distributions
795 from (I), black diamonds are forward ensemble fits from (F-H, left), and gray diamonds are
796 reverse ensemble fits from (F-H, right). At lower concentrations of ATP (1 and 10 μM), the
797 rate of detachment is limited by ATP association, corresponding to the reverse ensemble
798 fits, while at saturating ATP concentration (1000 μM), the detachment rate is limited by the
799 rate of ADP dissociation, corresponding to the forward ensemble fits. **(K)** Summary of rates
800 determined via single molecule optical trapping. Errors for detachment rates are 95%

801 confidence intervals. Errors for forward and reverse ensemble fits are standard errors of
802 the fits. *Detachment rates at 1000 μM ATP were best fit to the sum of 2 exponents. The
803 major component of the fit (67.8 s^{-1}) comprises 92.1% of the total with the remaining 7.9%
804 having a rate of 11.6 s^{-1}.
805
806 **Figure 4: Myo5 attachment lifetimes are substantially less force-dependent than**
807 **other known type I myosins**
808 An isometric optical force clamp was utilized to determine the force-sensitivity of the
809 detachment of Myo5 from actin. **(A)** Durations of individual actomyosin attachments as a
810 function of force, plotted on a semi-log scale **(B)** The solid black line shows the force
811 dependence of the detachment rates determined by MLE fitting of unaveraged points in A.
812 For illustration purposes, attachment durations from (A) were binned by force at every 10
813 points, averaged, and converted to rates. Best- fit parameters were determined by MLE
814 fitting and 95% confidence intervals were calculated via bootstrapping. The solid black line
815 is calculated from best fit parameters (k = 67.6 s^{-1}, d = 1.14 nm), while the gray shaded
816 region is the 95% confidence interval (k = 62.4-72.9 s^{-1}, d = 1.03-1.26 nm). All MLE fitting
817 was performed on unaveraged data and was corrected for instrument deadtime. **(C)** The
818 force dependent detachment rate of Myo5 (from panel B) plotted alongside the force
819 dependent detachment rates for Myo1b, Myo1c, and β-cardiac muscle myosin, Myh7. **(D)**
820 Power output for the same four myosins calculated over a range of forces by multiplying
821 the functions from (C) by the applied force F, and the step size and duty ratios of each
822 myosin.
823

824 **Figure S1: P21 Activated Kinase 1 (Pak1) phosphorylates Myo5 on S357**

825 Crude preparations of wild type and S357A Myo5 motor/lever constructs were mixed with
826 250 μM ATP including 20 μCi of ATPγP32 in kinase assay buffer (5 mM MOPS pH 7, 2.5 mM
827 β-glycerophosphate, 5 mM $MgCl_2$, 400 μM EDTA, 1 mM EGTA, 50 μM DTT) in either the
828 presence or absence of Pak1. Reactions were incubated at 25˚C for 60 minutes, then
829 quenched by adding an equal volume of 2x tris urea sample buffer (125 mM Tris pH 6.8,
830 6 M urea, 2% SDS, 0.1% bromophenol blue, 10% β-mercaptoethanol) and resolved on a
831 10% polyacrylamide gel. The gel was stained with Coomassie, then dried onto Whatman
832 paper and exposed to a storage phosphor screen (Amersham). The Coomassie-stained gel
833 was imaged on a standard photo scanner and the phosphor screen on a Typhoon gel imager
834 (Amersham). Note that there are differences in baseline labeling in the absence of added
835 kinase between the two different protein preps, but addition of Pak1 clearly results in
836 radiolabeling of wild type but not mutant Myo5.

837

838 **Movie S1: Motility assays with phosphorylated Myo5**

839 Rhodamine phalloidin-labeled actin filaments gliding over coverslips coated with a
840 concentration series of phosphorylated Myo5 protein in motility buffer with 1 mM ATP.
841 Movies were collected at 1 frame per second and are played back at 16 frames per second.

842

843

844 **Movie S2: Motility assays with unphosphorylated Myo5**

845 Rhodamine phalloidin-labeled actin filaments gliding over coverslips coated with a
846 concentration series of unphosphorylated Myo5 protein in motility buffer with 1 mM ATP.

847 Short movies of motility at 100 nM and 150 nM unphosphorylated Myo5 were collected

848 because no motility was observed. Movies at all other concentrations were collected at 1

849 frame every 4 seconds and are played back at 16 frames per second. The playback rate of

850 Movie S2 is four times faster than the playback rate of Movie S1.

Figure 1

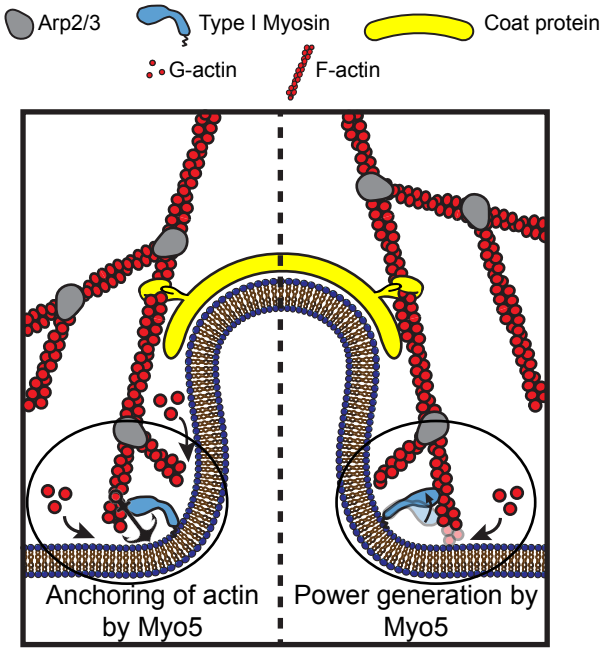
Arp2/3
Type I Myosin
Coat protein
G-actin
F-actin
Anchoring of actin by Myo5
Power generation by Myo5

Figure 2

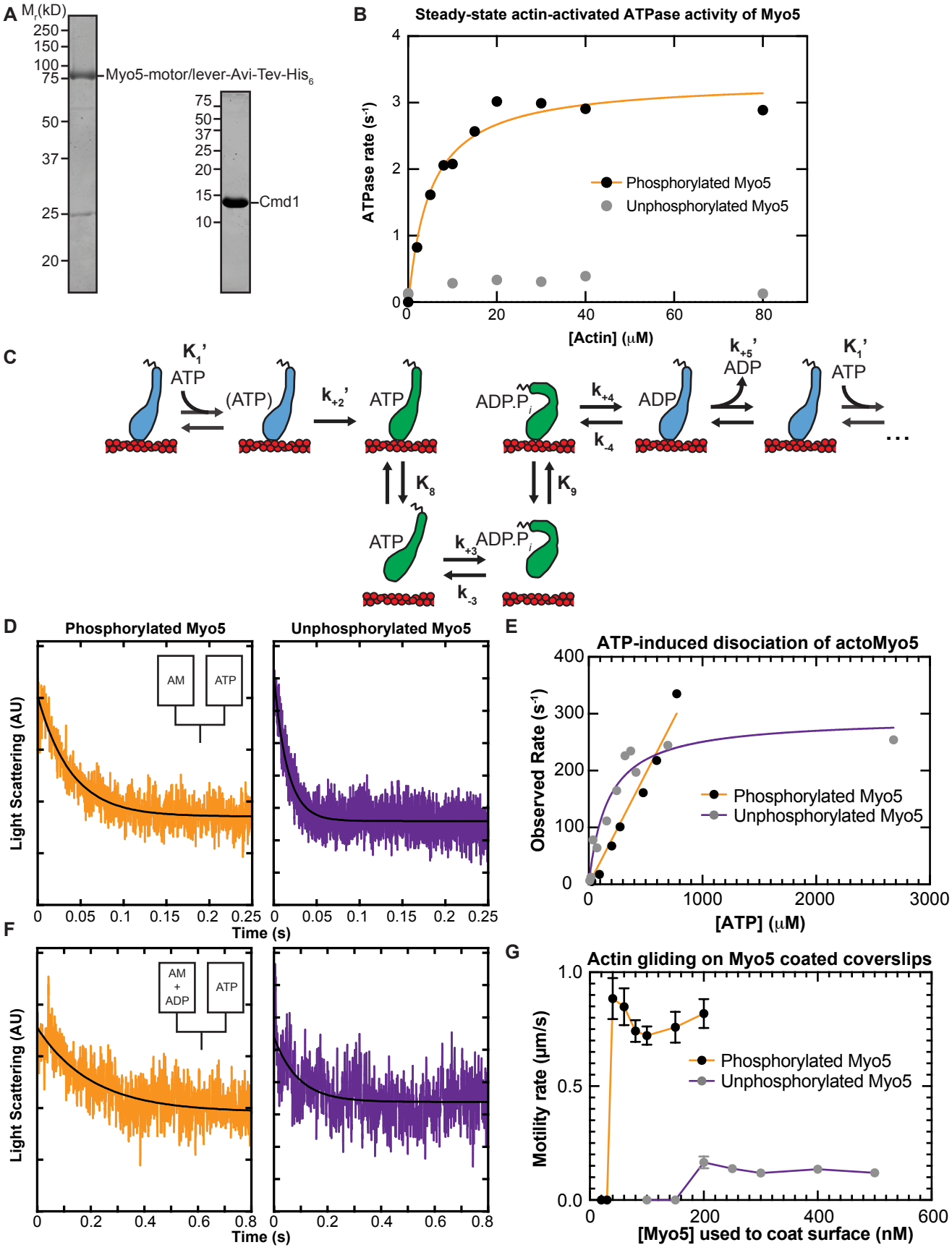
A
Mr(kD)
250
150
100
75
50
37
25
20
Myo5-motor/lever-Avi-Tev-His6
75
50
37
25
20
15
10
Cmd1
B
Steady-state actin-activated ATPase activity of Myo5
ATPase rate (s-1)
[Actin] (μM)
Phosphorylated Myo5
Unphosphorylated Myo5
C
K1'
ATP
(ATP)
k+2'
ATP
ADP.Pi
k+4
k-4
ADP
k+5'
ADP
K1'
ATP
K8
K9
ATP
k+3
ADP.Pi
k-3
D
Phosphorylated Myo5
Unphosphorylated Myo5
AM
ATP
Light Scattering (AU)
Time (s)
E
ATP-induced disociation of actoMyo5
Observed Rate (s-1)
[ATP] (μM)
Phosphorylated Myo5
Unphosphorylated Myo5
F
AM + ADP
ATP
Light Scattering (AU)
Time (s)
G
Actin gliding on Myo5 coated coverslips
Motility rate (μm/s)
[Myo5] used to coat surface (nM)
Phosphorylated Myo5
Unphosphorylated Myo5

Table 1: Rate and equilibrium constants of the Myo5 ATPase cycle

	Phosphorylated Myo5	Unphosphorylated Myo5
Steady-state actin-activated ATPase		
V_{max} (s^{-1})	3.3 (± 0.15)	ND
K_{ATPase} (μM)	5.1 (± 0.88)	ND
ATP binding		
K_1' (μM^{-1})	ND	0.006 (± 0.0016)
k_{+2}' (s^{-1})	≥ 335	290 (± 24)
$K_1'k_{+2}'$ (μM^{-1} s^{-1})[a]	0.39 (± 0.017)[b]	1.1 (± 0.28)[c]
ADP release		
k_{+5}' (s^{-1})	74 (± 2.0)	107 (± 5.9)

[a]Determined from a linear fit of the unbinding rates. [b]Linear fit of all data for Phosphorylated Myo5 in Fig. 2E. [c]Linear fit of observed rates below 100 μM ATP for Unphosphorylated Myo5 in Fig 2E. ND: Not Determined.

Figure 3

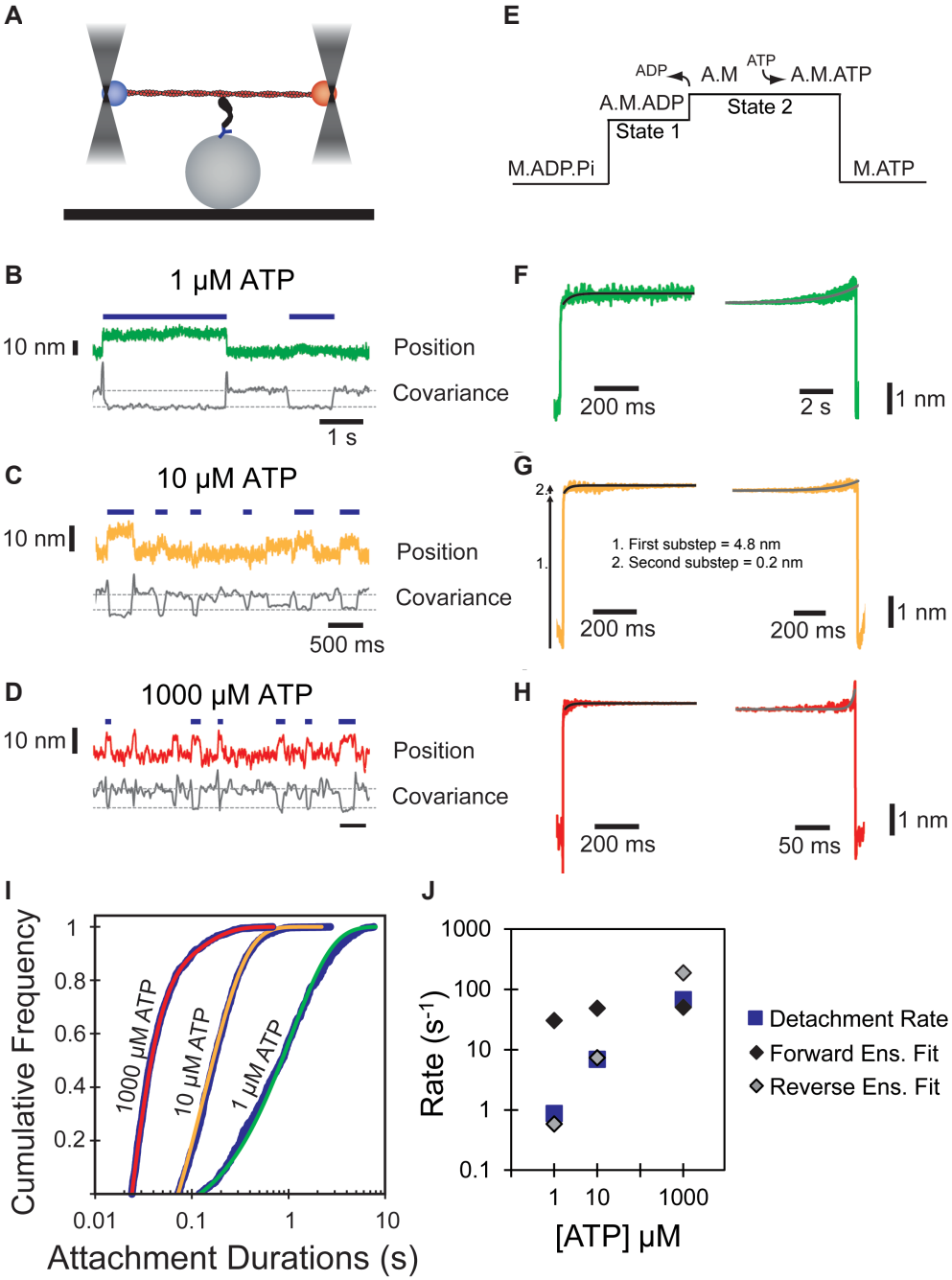

K

Summary of rates determined during single molecule optial trapping

[ATP] μM	Detachment Rate (s^{-1})	Forward Ensemble Fit (s^{-1})	Reverse Ensemble Fit (s^{-1})
1	0.88 (+/- 0.07/0.07)	>30	0.59 (+/- 0.003)
10	6.9 (+/- 0.49/0.46)	49 (+/- 1.6)	7.3 (+/- 0.1)
1000	67.8* (+/- 11.9/8.7)	50 (+/- 0.2)	>187

Figure 4

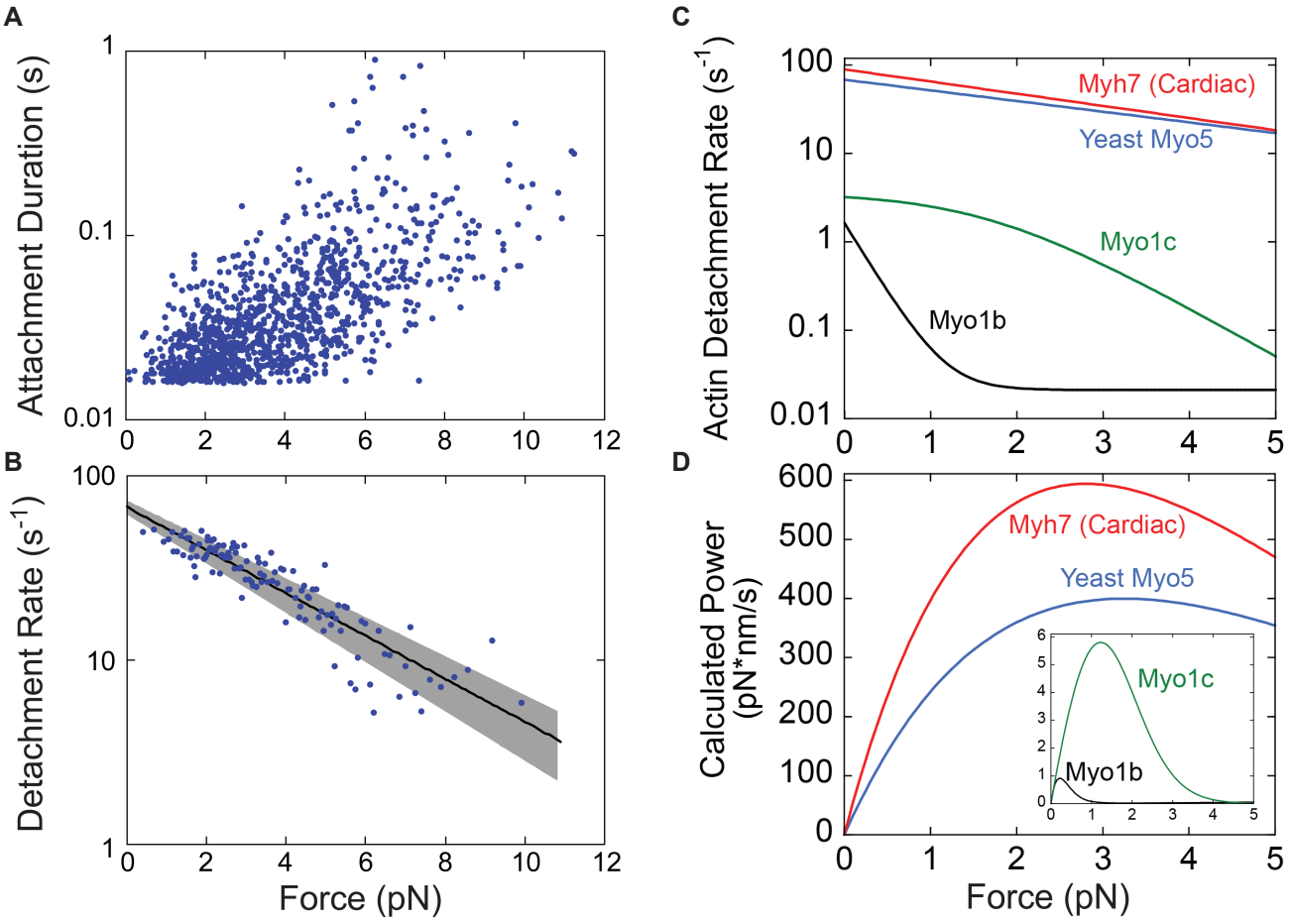
A
Attachment Duration (s)
1
0.1
0.01
0
2
4
6
8
10
12
B
Detachment Rate (s-1)
100
10
1
Force (pN)
C
Actin Detachment Rate (s-1)
100
10
1
0.1
0.01
Myh7 (Cardiac)
Yeast Myo5
Myo1c
Myo1b
0
1
2
3
4
5
D
Calculated Power (pN*nm/s)
600
500
400
300
200
100
0
Myh7 (Cardiac)
Yeast Myo5
Myo1c
Myo1b
Force (pN)